



Technical Notes

A reaction plane detector for PHENIX at RHIC[☆]

E. Richardson^{d,*}, Y. Akiba^{f,g}, N. Anderson^d, A.A. Bickley^b, T. Chujo^j, B.A. Cole^c, S. Esumi^j, J.S. Haggerty^a, J. Hanks^c, T.K. Hemmickⁱ, M. Hutchison^d, Y. Ikeda^j, M. Inaba^j, J. Jia^{a,h}, D. Lynch^a, Y. Miake^j, A.C. Mignerey^d, T. Niida^j, E. O'Brien^a, R. Pak^a, M. Shimomura^j, P.W. Stankus^e, T. Todoroki^j, K. Watanabe^j, R. Wei^h, W. Xie^g, W.A. Zajc^c, C. Zhang^e

^a Physics Department, Brookhaven National Laboratory, Upton, NY 11973-5000, USA

^b University of Colorado, Boulder, CO 80309, USA

^c Columbia University, New York, NY 10027 and Nevis Laboratories, Irvington, NY 10533, USA

^d University of Maryland, College Park, MD 20742, USA

^e Oak Ridge National Laboratory, Oak Ridge, TN 37831, USA

^f RIKEN Nishina Center for Accelerator-Based Science, Wako, Saitama 351-0198, Japan

^g RIKEN BNL Research Center, Brookhaven National Laboratory, Upton, NY 11973-5000, USA

^h Chemistry Department, Stony Brook University, SUNY, Stony Brook, NY 11794-3400, USA

ⁱ Department of Physics and Astronomy, Stony Brook University, SUNY, Stony Brook, NY 11794, USA

^j Institute of Physics, University of Tsukuba, Tsukuba, Ibaraki 305, Japan

ARTICLE INFO

Article history:

Received 3 December 2010

Received in revised form

11 January 2011

Accepted 11 January 2011

Available online 19 January 2011

Keywords:

Scintillator

Paddle

Heavy-ions

Reaction plane

PHENIX

RHIC

ABSTRACT

A plastic scintillator paddle detector with embedded fiber light guides and photomultiplier tube readout, referred to as the Reaction Plane Detector (RXNP), was designed and installed in the PHENIX experiment prior to the 2007 run of the Relativistic Heavy Ion Collider (RHIC). The RXNP's design is optimized to accurately measure the reaction plane (RP) angle of heavy-ion collisions, where, for mid-central $\sqrt{s_{NN}} = 200$ GeV Au+Au collisions, it achieved a 2nd harmonic RP resolution of ~ 0.75 , which is a factor of ~ 2 greater than PHENIX's previous capabilities. This improvement was accomplished by locating the RXNP in the central region of the PHENIX experiment, where, due to its large coverage in pseudorapidity ($1.0 < |\eta| < 2.8$) and ϕ (2π), it is exposed to the high particle multiplicities needed for an accurate RP measurement. To enhance the observed signal, a 2-cm Pb converter is located between the nominal collision region and the scintillator paddles, allowing neutral particles produced in the heavy-ion collisions to contribute to the signal through conversion electrons. This paper discusses the design, operation and performance of the RXNP during the 2007 RHIC run.

© 2011 Elsevier B.V. All rights reserved.

1. Introduction

The Reaction Plane Detector (RXNP) was installed in the PHENIX experiment [1], located at Brookhaven National Laboratory's Relativistic Heavy Ion Collider (RHIC) [2], prior to the 2007 RHIC run. The RXNP is a scintillator paddle detector embedded with optical fiber light guides connected to photomultiplier tubes (PMT's), with the design purpose of accurately measuring the reaction plane (RP) angle of heavy ion collisions, which is defined by the impact parameter and beam axis, and whose angle (Ψ_R) is determined with respect to a constant arbitrary angle from the laboratory coordinate system. To increase the accuracy of this measurement a 2-cm lead (Pb) converter is located directly in

front of the scintillators with respect to the nominal collision region, thereby allowing neutral particles to contribute to the signal through conversion electrons, as well as increasing the overall particle flux through the scintillators and thus increasing energy deposition. However, due mainly to finite particle statistics and detector granularity, it is impossible to know Ψ_R with absolute certainty, thus its experimental measurement is referred to as the event plane (EP) angle.

Measuring the EP angle is important in heavy-ion collisions because it allows for the study of how the collective geometry of the participating nucleons affects the emitted particles' angular abundance, such as in elliptic flow (v_2), the path length dependence of their energy loss through the medium, as well as being an important component when comparing heavy-ion and p+p collisions. Such studies provide a wealth of information about the properties of the created matter. For instance, identified particle scaling in v_2 measurements has shown that the medium exhibits quark degrees of freedom [3,4], thereby lending strong evidence

[☆] For the PHENIX Collaboration.

* Corresponding author.

E-mail address: ericr@umd.edu (E. Richardson).

to the formation of a quark gluon plasma (QGP). These v_2 measurements are well described by hydrodynamic models at low transverse momentum (p_T) [5], suggesting the medium behaves like an ideal fluid. Furthermore, v_2 studies, along with the geometrical dependence of jet suppression [6,7], which also relies on the event-by-event measurement of the EP angle, were an important basis for the conclusion in the RHIC white papers [8–11] that a highly dense, strongly interacting medium is formed in RHIC's Au+Au collisions when the center-of-mass energy per nucleon pair ($\sqrt{s_{NN}}$) is 200 GeV. In addition, many other measurements rely on measuring the EP angle, including other harmonic flow measurements, CP violation, HBT, and R_{AA} [12–17].

The RXNP is used to measure the EP angle from the azimuthal asymmetry of the produced particle distribution, referred to as anisotropic flow, which can be described by the Fourier expansion [18]

$$\frac{d(wN)}{d(\phi - \Psi_R)} = \frac{\langle wN \rangle}{2\pi} \left(1 + \sum_n 2v_n \cos[n(\phi - \Psi_R)] \right) \quad (1)$$

where n represents the n th harmonic of the distribution, N is the number of particles measured, ϕ is the particle angle, w are weights, and v_n is the anisotropy parameter representing the magnitude of the flow signal. From this same anisotropy the EP angle is measured using

$$\Psi_n = \frac{1}{n} \tan^{-1} \left(\frac{Y_n = \sum_i w_i \sin(n\phi_i)}{X_n = \sum_i w_i \cos(n\phi_i)} \right) \quad (2)$$

where Ψ_n is the measured EP angle from the n th harmonic particle distribution and X_n and Y_n are the event flow vectors.

Before the installation of the RXNP, PHENIX measured Ψ_n using its Beam Beam Counter (BBC) detectors [19], which, for mid-central $\sqrt{s_{NN}} = 200$ GeV Au+Au collisions, had a 2nd harmonic EP resolution, defined as $\langle \cos[n(\Psi_n - \Psi_R)] \rangle$, of ~ 0.4 , where 1.0 would denote a perfect resolution. This resolution proved sufficient for studying abundant low p_T particles, but was insufficient for making new discoveries with photons and rarer probes such as J/ψ and high p_T particles. Therefore, a better EP resolution was required to increase the physics capabilities of a data set by yielding smaller error bars during analysis. The RXNP was designed and built to fulfill this need.

Reported here are the simulations and experimental tests done to optimize the RXNP's design and material compositions. The final detector geometry is also discussed, along with its online performance during the 2007 RHIC run where Au nuclei were collided at $\sqrt{s_{NN}} = 200$ GeV. Finally, a discussion of the detector's calibrations and performance is included.

2. Simulations and testing

The RXNP was designed to optimize the resolution of the 2nd harmonic EP measurement, while not interfering with the location and particle acceptance of existing PHENIX sub-systems. One contributing factor that strongly influences the resolution is the particle multiplicity that is incident on the detector, where a large multiplicity is desirable. This can be maximized by designing the RXNP to include a large pseudorapidity (η) coverage, while placing it close to the nominal vertex position. Within the PHENIX experiment, shown in Fig. 1, this region is largely occupied by existing sub-systems, magnets and support structures. After considering the space available for a new detector, it was decided that the RXNP would be composed of two mirror image halves of radiating paddles located approximately ± 40 cm from the nominal vertex position and attached to the face of the central magnet's copper (Cu) nosecones.

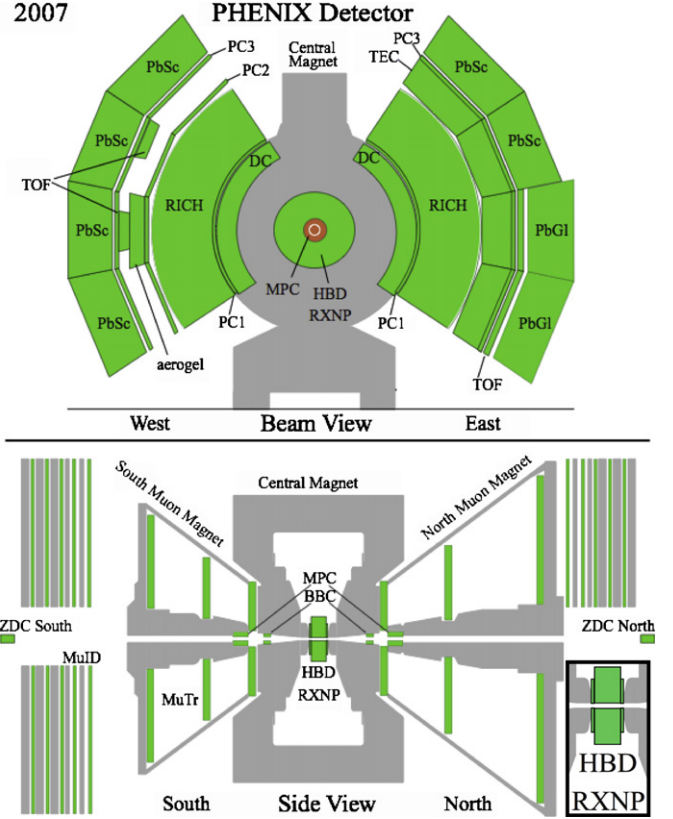


Fig. 1. PHENIX detector configuration for the 2007 RHIC run. As shown in the Side View insert (bottom right), the RXNP is sandwiched between the central magnet and the HBD.

This location provided several design challenges including: (1) there being only 7 cm of available space between each nosecone and the soon to be installed Hadron Blind Detector (HBD) [20] and (2) the detector had to be able to operate effectively in the high magnetic field environment of PHENIX's central region, where the field strength can be as high as 1 Tesla. In order to satisfy these requirements and answer many outstanding design questions, including material composition, converter effectiveness, and signal readout, extensive studies were performed.

Some of these issues were addressed in GEANT3 [21] based simulations using realistic v_2 and multiplicity distributions in η , p_T and ϕ for $\sqrt{s_{NN}} = 200$ GeV Au+Au collisions. The RXNP was modeled as two scintillating disks surrounding the beam pipe and evenly divided into 8 segments in ϕ , while located at either ± 34 or ± 39 cm from the nominal vertex. The η coverage for these simulations varied, but was always between $0.8 < |\eta| < 2.8$. Placed immediately in front of the scintillators was a similarly shaped metal converter whose purpose was to increase the EP resolution through the means described in Section 1.

The effectiveness of the converter in accomplishing this is seen in Fig. 2, which shows resolution vs. centrality, i.e. the percent of collisions having more geometrical overlap than the current collision. Here an average of 16% increase in the 2nd harmonic EP resolution is seen when all the charged particles of a collision are used to measure the EP, compared to using only primary charged particles. A major reason for this improvement is shown in Fig. 3 where the primary, secondary and background particle distributions are shown with respect to Ψ_R . With no converter (a) a strong flow signal from primary particles is seen, but this is diluted by the secondary particles showing a nearly flat distribution. However, if a 0.5-cm brass converter is added, as seen in (b), the secondary particles not only increase in number due to the production of

conversion electrons, as demonstrated by a similar simulation in Table 1, but they also carry a strong flow signal themselves that originates from the distribution of the parent particles, thereby reinforcing the flow signal from the primary particles. The addition of a converter was also shown to reduce the low energy background.

Increasing converter thickness was also shown to increase the 2nd harmonic EP resolution, as seen in Table 2, while increasing scintillator thickness was shown to give a better correlation between the number of particle hits and energy deposition, as depicted in Fig. 4. To optimize the converter and scintillator thickness within the constraints of the limited space available between the nosecone and HBD, it was decided to restrict the thickness of the converter and scintillator to 2 cm each. Therefore, 2-cm thick brass, Pb and tungsten (W) converters were simulated with a 2-cm thick scintillator to compare energy deposition, as shown in Fig. 5, and their effect on the 2nd harmonic EP resolution for mid-central collisions, which were found to be 0.70, 0.74 and 0.76, respectively. In both cases W performed best, but only marginally so compared to

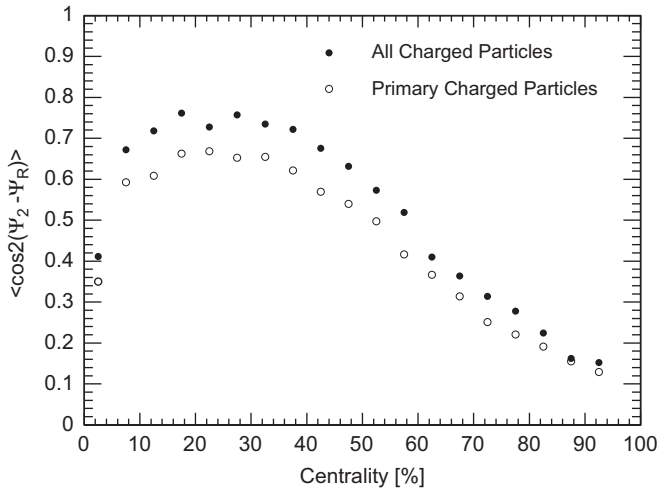


Fig. 2. Second harmonic EP resolution vs. centrality of the RXNP using a GEANT3 based simulation, where open circles pertain to only primary charged particle hits and closed circles are for all charged particle hits. Here the effectiveness of the converter is demonstrated by the secondary charged particles increasing the detector's resolution compared to using only primary charged particles. Also notice the resolution varies as a function of centrality, where it is at a maximum between 20% and 30%. This is caused by a combination of changing event multiplicity and ν_2 signal.

Pb, which is significantly less expensive. Therefore, Pb was chosen as the converter material.

The optimum radiator ϕ segmentation for the 2nd harmonic EP resolution was also studied. Fig. 6 shows that the resolution improves only marginally above 8 segments; however, to protect against failing segments it was decided to partition the detector into 12 paddles in ϕ . The RXNP was further divided into two radial sections covering $1.0 < |\eta| < 1.5$ (outer ring) and $1.5 < |\eta| < 2.8$ (inner ring) as a result of a series of simulations incorporating the PHENIX central arm spectrometers ($|\eta| < 0.35$) that showed a centrality and η dependent fake ν_2 signal from jets when using the EP of the RXNP. These studies showed that the largest bias occurs in peripheral events, shown in Fig. 7, and the closer in proximity the RXNP's η coverage is to the central arms. This bias can result from back-to-back di-jet correlations, as well as correlated particle production from the near-side jet cone, which can have a size of 0.7 units in η .

Therefore, to minimize the impact of this bias on a wide range of physics analyses, the RXNP was divided into two η sections resulting in the inner ring section experiencing only a minimal bias effect. This added flexibility was proven effective in Ref. [22], where only the inner ring was used in measuring the ν_2 of high p_T π^0 's, and in Ref. [23], which used both η sections in examining the η dependence of non-flow effects.

Avalanche photodiodes (APD's) and PMT's were considered for signal readout. APD's have several advantages over PMT's,

Table 1

Charged particles per segment using different thickness brass converters.

Converter thickness	Primary	Secondary	Total
No converter	151	78	229
1.5 cm	132	340	472
4 cm	103	723	826

Table 2

Simulated 2nd harmonic EP resolution for mid-central events using different thickness converters and a 2-cm thick scintillator.

Converter thickness (cm)	0.0	1.0	2.0	4.0	8.0
Brass	0.53	0.65	0.71	0.76	0.80
Pb	0.53	0.73	0.75	0.75	0.68

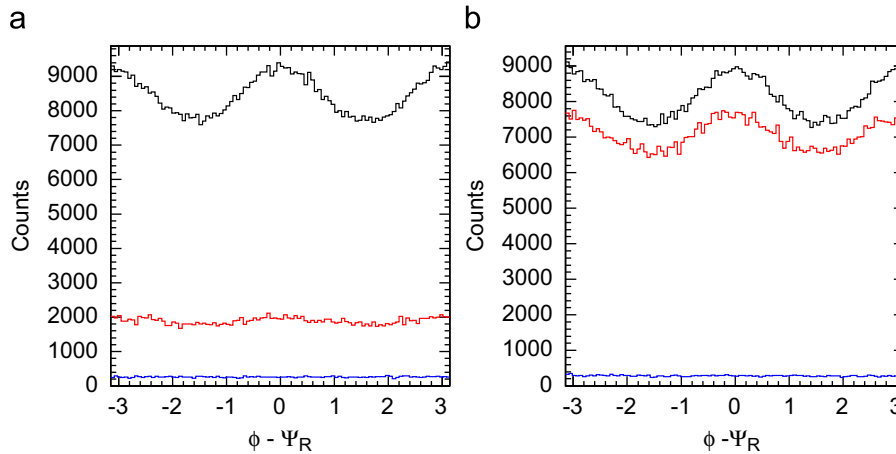


Fig. 3. Particle distribution with respect to Ψ_R for primary (top, black), secondary (middle, red) and background (bottom, blue) particles without (a) and with (b) a converter. Without the converter the secondary particles have a nearly flat distribution, but with a 0.5 cm brass converter the secondary particles exhibit a strong flow signal, thereby reinforcing the flow signal from the primary particles. (For interpretation of the references to color in this figure legend, the reader is referred to the web version of this article.)

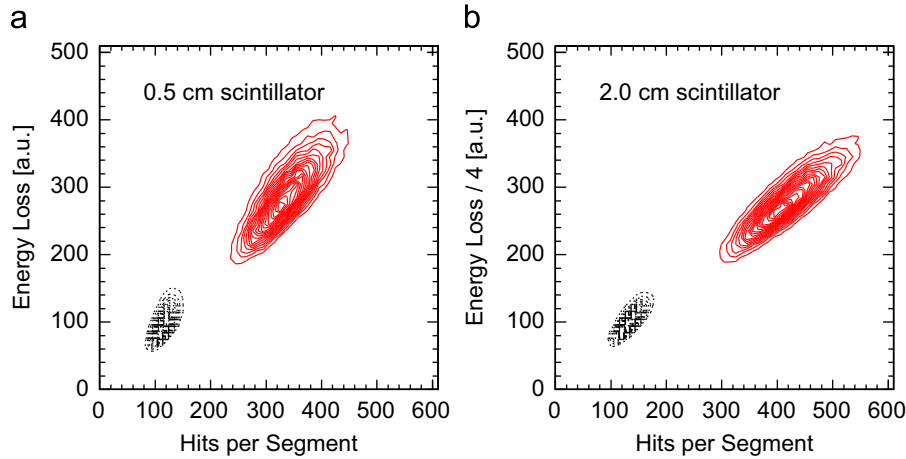


Fig. 4. Number of particle hits per scintillator segment vs. energy loss. The scintillator thickness is 0.5 and 2.0 cm for (a) and (b), respectively. The dotted contour lines (black) use no converter, while the solid lines (red) use a 2.0-cm brass converter. Notice the energy loss in (b) is divided by 4. Both with and without the converter, the correlation is better with the thicker scintillator. (For interpretation of the references to color in this figure legend, the reader is referred to the web version of this article.)

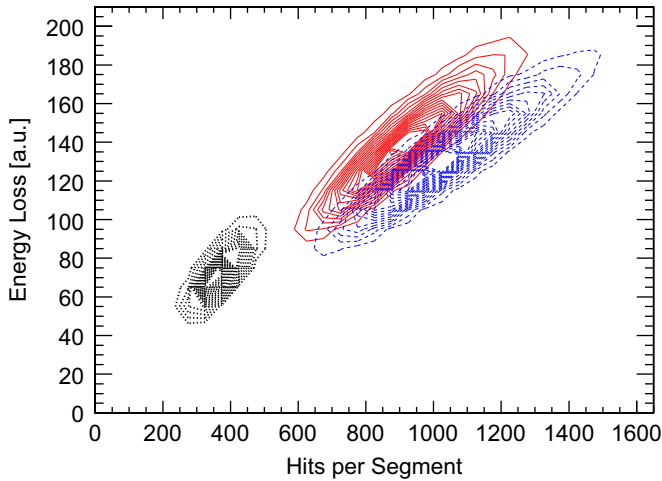


Fig. 5. Particle hits per scintillator segment vs. energy loss using 2.0-cm brass (dotted, black), Pb (solid, red) and W (dashed, blue) converters. Tungsten provides the best hit to energy loss correlation, but only marginally so over Pb, which is significantly less expensive. In all cases a 2-cm scintillator was used. (For interpretation of the references to color in this figure legend, the reader is referred to the web version of this article.)

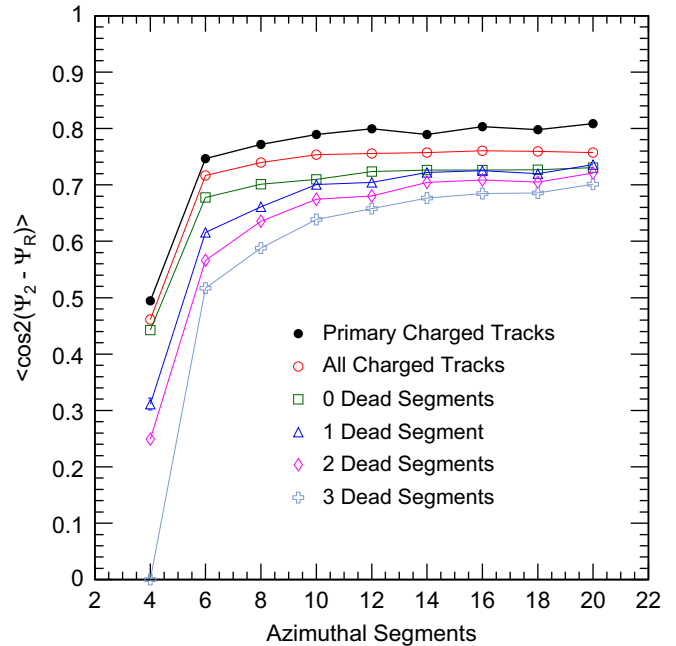


Fig. 6. Dependence of the 2nd harmonic EP resolution of mid-central collisions on the azimuthal segmentation of the RXNP resolution. The closed circles use only the number of primary charged particles in each segment as the weight, with each particle having a weight of 1. The resolution for the open circles is similarly calculated, but uses all charged particles (primary, secondary and background). The square, triangle, diamond and cross data points all calculate the resolution using the energy deposition into the scintillators from charged particles as the weighting factor, while at the same time having 0, 1, 2 or 3 dead scintillator segments, respectively. In all cases a 2-cm scintillator and 2-cm brass converter were used.

including being unaffected by magnetic fields, significantly cheaper and allowing for a simpler design by jettisoning the need for light guides. However, after performing calculations and bench tests, it was confirmed that the signal to noise ratio from APD's was insufficient for this application. Therefore, it was decided to pursue a PMT design.

To confirm that PMT's could function well in PHENIX's strong magnetic field and to investigate an optimal radial position and angular orientation with respect to the field lines, a series of magnetic field tests were performed. One of these tests involved constructing and positioning a test stand in PHENIX's central region that simultaneously held 2 sets of 4 PMT's, separated by 120° at radial positions where their gains were predetermined to be best: 80, 90, 110 and 130 cm. Hamamatsu R5924 fine mesh PMT's were used, which are specifically designed to operate in a high magnetic field environment. Using an LED pulser, each tube's gain was recorded at zero and full field for PHENIX's “++” and “+−” field configurations. In addition, because the region in which the RXNP was to be installed is near the magnetic field

return, the field lines exhibit non-uniform behavior that is not well known. Moreover, with PMT performance in a magnetic field known to be sensitive to the alignment of the tube with respect to the field lines, two configurations were tested for each field setting: PMT's aligned parallel and at 30° to the beam pipe. The results of this test are shown in Table 3, where the numbers are averaged from the two PMT's located at each distance. Based largely on these results and the fact that the magnetic field would be in the “+−” configuration for the 2007 run, it was decided the PMT's would be placed parallel to the beam pipe at a radial

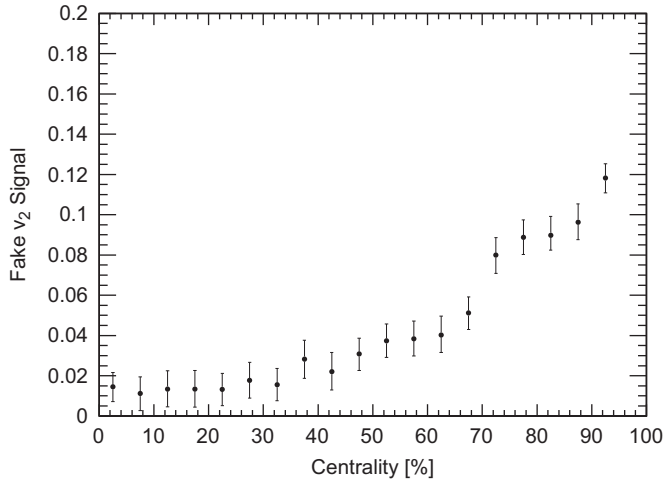


Fig. 7. Simulated fake ν_2 signal from jets with respect to centrality in the PHENIX central arm spectrometers ($|\eta| < 0.35$) when using the EP calculated from the RXNP and requiring each event's leading hadron to have a $p_T > 6$ GeV/c. 1σ statistical error bars are also shown.

Table 3

Fraction of PMT gain observed at full field compared to zero field.

Distance (cm)	"++" 30°	"+-" 30°	"++" Parallel	"+-" Parallel
80	0.61	0.00	0.76	0.56
90	0.39	0.33	0.78	0.23
110	0.50	0.32	0.96	0.54
130	0.44	0.35	0.85	0.66

distance of 130 cm. Here they would experience a magnetic field strength of ~ 0.66 T (~ 0.61 T) for the "++" ("+-") field configurations.

With much of the design solidified, the remaining element to be determined was the radiator and light guide configuration. This was resolved through beam tests performed at KEK-PS in Japan using a momentum selected charged particle beam. The purpose of these tests were to examine different radiator (scintillator vs. Cherenkov) and light guide (solid vs. embedded fiber) combinations. These tests showed that, although the solid light guide resulted in more light collection, it also had a signal size that was dependent on the incident particle's position in the radiator, as seen before in Ref. [24], which would likely worsen the EP resolution. This effect was significantly less pronounced using the embedded fibers. This, combined with the fibers reasonable light collection and flexibility in positioning and grouping PMT's, led to their selection. The Cherenkov radiator was eliminated because it yielded too small a signal when used with embedded fibers, while the scintillator signal was reasonable. Thus scintillator radiators with embedded fiber light guides were chosen for the RXNP.

3. Design and geometry

The RXNP is composed of two sets of 24 scintillators, a north (N) and a south (S), located ± 39 cm from the nominal vertex position with the S arm being located in the negative direction. The scintillators are arranged perpendicular to and surround a 10-cm diameter beam pipe in 2 concentric rings (inner, outer), with each ring having 2π coverage and 12 equally sized segments in ϕ . All scintillators are trapezoidal in shape, 2-cm thick, made of EJ-200 material from Eljont Technology (equivalent to BC408) and individually wrapped with an inner layer of aluminized mylar sheeting for

light reflection and an outer layer of black plastic for light tightness. A schematic diagram showing the arrangement of the scintillators and their sizes is shown in Fig. 8, with the edges of the inner ring positioned at radial distances of 5 and 18 cm from the ion beam covering $1.5 < |\eta| < 2.8$. Uninterrupted coverage continues outward with the outer ring to 33 cm or $|\eta| = 1.0$. The length of the inner and outer edges of the inner scintillators are 2 and 9 cm, respectively, with the outer edge of the outer scintillators being 17 cm.

Each 24 scintillator set is housed in 4 identical aluminum structures each consisting of a tray covering 90° in ϕ with a support arm extending radially ~ 80 cm. As shown in Fig. 9(a), each tray contains three compartments for an inner and outer scintillator with each scintillator having wavelength shifting fiber light guides embedded into its surface every 0.5 cm and running its entire length. To allow the inner scintillator's fibers to run radially out the back of the tray in tandem with the outer scintillator's fibers, an offset between the two is created by placing a 2-mm plastic spacer underneath the inner scintillator, as shown in Fig. 9(b). On top of the scintillators sits another 2-mm spacer for protection, followed by a 2-cm thick converter composed of 98% Pb doped with 2% antimony to increase hardness.

As the fibers exit each scintillator they are individually sheathed in black plastic tubing for light tightness, bundled together inside flexible plastic tubing for stability and protected by an Al cover. They then run the length of the support arm fastened by plastic ties and protected by two more Al covers. At the end of the arm each scintillator's fibers are unsheathed from their individual tubing, yet still encased in the larger flexible tubing, bundled together into a plastic end cap and attached to a "cookie" covering the face of a PMT. Here the cookie guides the light from the fibers into the PMT using a 45° reflective surface to bend the light a total of 90° . Along with black tape, a custom built Delrin cap is used to fasten the cookie onto the PMT and make the connection light tight. Each PMT is then fastened to the end of the arm and positioned parallel to the beam pipe, giving each quadrant a length of ~ 124 cm.

Hamamatsu R5543 3 in. fine mesh PMT's are used to measure the signal. Although not the same type of PMT used in the original

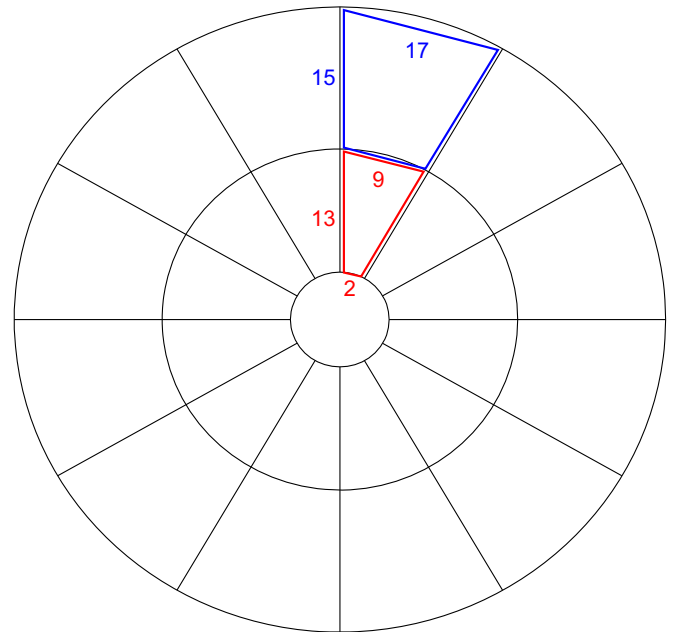


Fig. 8. Schematic diagram illustrating the arrangement of the inner (red) and outer (blue) scintillator rings. The length of each scintillator side is shown in centimeters. (For interpretation of the references to color in this figure legend, the reader is referred to the web version of this article.)

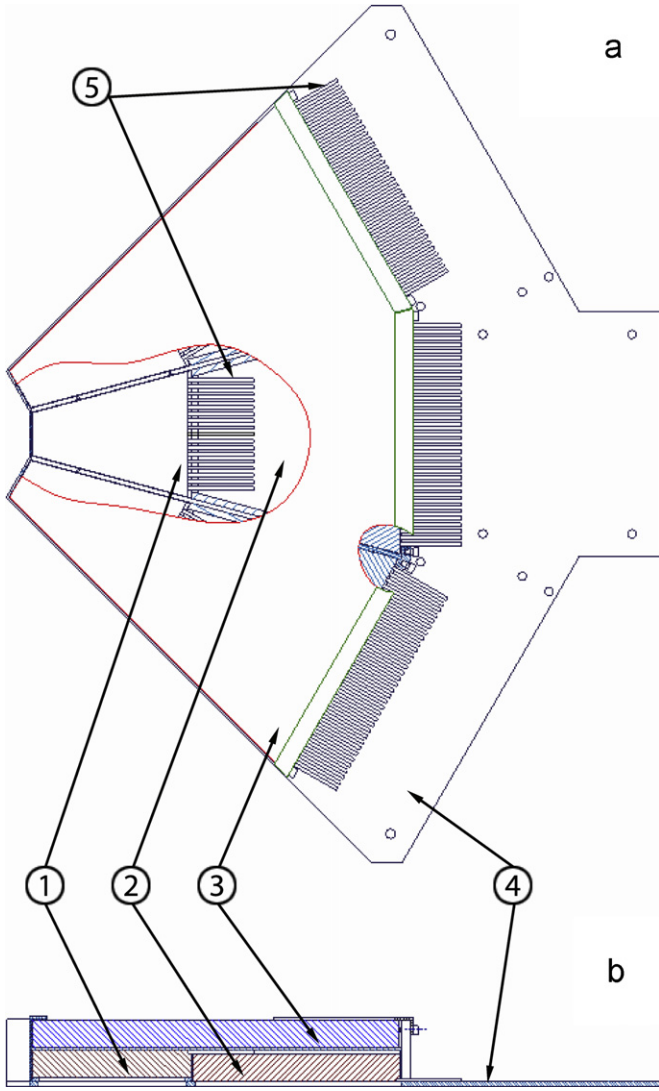


Fig. 9. (a) shows a top view of an assembled tray with a cutout of the Pb converter (3) showing the inner (1) and outer (2) scintillators underneath in their compartments with their optical fibers (5) emerging to their rear. (4) identifies the aluminum tray. (b) shows a side view of an assembled tray with the Pb converter above the scintillators. Notice the plastic spacer directly underneath the inner scintillator, offsetting it from the outer scintillator, allowing its fiber light guides to exit the tray.

magnetic field tests discussed in Section 2, these PMT's are also designed to operate in a high magnetic field with similar behavior expected. Moreover, these PMT's did undergo their own magnetic field testing as mentioned in Section 4. Once assembled each quadrant was fastened to the nosecone, giving the tray portion of the assembly a total thickness of ~ 5 cm. A picture of the RXNP's north half after installation is shown in Fig. 10.

4. Online performance and calibrations

Prior to final assembly and installation, each PMT was tested for noise, signal linearity and signal strength in and outside a magnetic field. After installation one PMT in the south arm became disabled prior to the 2007 RHIC run, decreasing the detector acceptance to $\sim 98\%$ of design, which remained throughout the run. Fig. 11 shows a typical ADC spectrum from a PMT during min-bias data taking, where, at the maximum edge of the distribution, several hundred

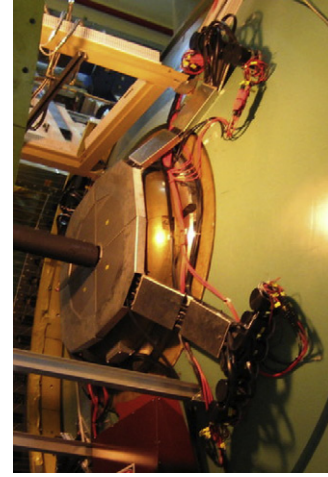


Fig. 10. Picture of the RXNP's north half installed on the Cu nosecone of PHENIX's central magnet prior to the installation of the HBD.

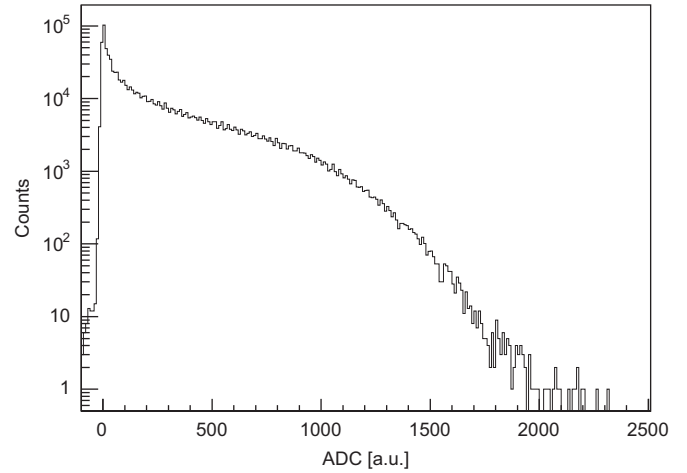


Fig. 11. Typical raw ADC spectrum of a PMT from min-bias data. The distribution results from frequent peripheral (low multiplicity) and rare central (high multiplicity) interactions, which are proportional to the geometrical cross-section.

charged particles, including conversion electrons, are measured in the scintillator segment. The dynamic range of the ADC is 12 bits or 4096 quantized units, of which ~ 2000 are typically used.

The gain of the tubes was monitored throughout the run and was found to decrease over time, as shown in Fig. 12, with no pattern seen regarding scintillator location. During the 2008 and 09 RHIC runs similar voltages were used while colliding species of p+p and d+Au at the same energy, along with p+p at $\sqrt{s_{NN}} = 500$ GeV. The p+p data showed no signal degradation, while for d+Au some degradation was seen in both RXNP arms, although not as severe as with Au+Au. For the 2010 RHIC run, where Au+Au was again collided at $\sqrt{s_{NN}} = 200$ GeV, the RXNP high voltage was increased to counter the loss in gain observed in 2007. The result was a comparable, although not quite as severe degradation to that of 2007. The cause of the gain loss remains unexplained, but appears related to the use of heavy-ions at higher energies, since no degradation was seen during the 2010 lower energy ($\leq \sqrt{s_{NN}} = 62.4$ GeV) Au+Au running period.

The observed signal degradation has a negligible effect on the RXNP's 2nd harmonic EP resolution, except in the most peripheral events where the change was less than 5%. The effect of the removal of the west half of the HBD $\sim 1/3$ rd through the run was

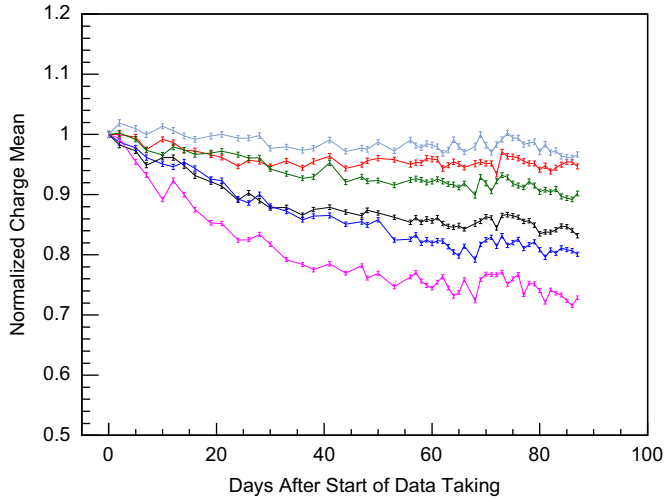


Fig. 12. Normalized mean gain values of 6 representative PMT's taken periodically during the 2007 RHIC run. Each PMT is normalized to its own charge mean at the start of data taking. 1σ statistical error bars are also shown.

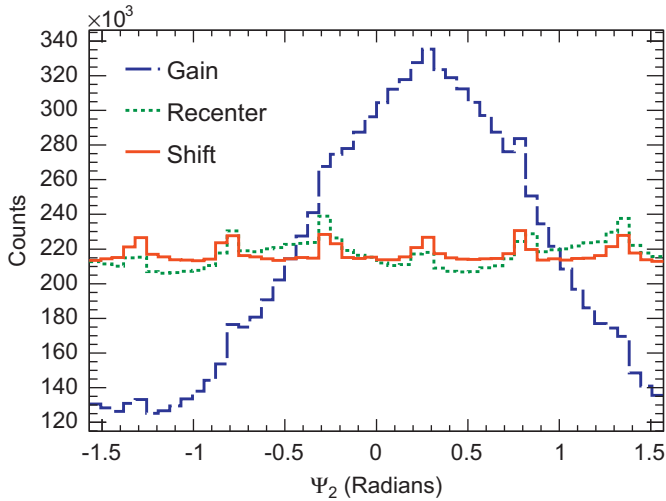


Fig. 13. Second harmonic EP distribution of min-bias events from a typical run after each calibration step. The dashed line (blue) is after the gain correction, dotted line (green) is after recentering and the solid line (red) is after angular shifting. (For interpretation of the references to color in this figure legend, the reader is referred to the web version of this article.)

also examined and found to be negligible for central events, but did increase the resolution of peripheral events by up to 10%.

After pedestal subtraction three calibrations were performed on a run by run basis to flatten the EP angle distribution, which, by definition, should be flat since the RP from the two colliding nuclei has an equal probability of occurring at any angle. However, due to effects such as the broken PMT, unequal PMT gains, and beam offset, the EP angular distribution from the raw data was not flat. To correct this, each PMT's gain was first calibrated to have the same mean ADC value. The second step recentered the X_n and Y_n event flow vector distributions to zero along with adjusting their width to unity by [18]

$$X_n^{corr} = \frac{X_n - \langle X_n \rangle}{\sigma_{X_n}} \quad (3)$$

$$Y_n^{corr} = \frac{Y_n - \langle Y_n \rangle}{\sigma_{Y_n}} \quad (4)$$

where X_n^{corr} and Y_n^{corr} are the corrected flow vectors and σ_{X_n} and σ_{Y_n} are the uncorrected distribution widths. The third step fits a Fourier expansion to the modified distribution and performs an event-by-event shifting of the angles using [25]

$$\Psi_n^{corr} = \Psi_n + \frac{1}{n} \sum_i \frac{2}{i} [-\langle \sin(in\Psi_n) \rangle \cos(in\Psi_n) + \langle \cos(in\Psi_n) \rangle \sin(in\Psi_n)] \quad (5)$$

where Ψ_n^{corr} is the corrected and final EP angle. The result from each of these steps for the 2nd harmonic EP is shown in Fig. 13. Notice the final distribution has six remaining “spikes”. These spikes result from the flattening of the distribution to the 5th harmonic in the final calibration step, along with the combination of finite detector granularity and low multiplicity peripheral events. For these events it is possible for only one paddle to be hit causing its angular center to be assigned as that event's EP angle. This causes an overrepresentation of that angle in the EP distribution that is not eliminated by the calibrations. However, these spikes do disappear for event centralities $< 70\%$.

5. EP resolution

The RXNP can measure the EP angle from nine different detector segment combinations; N+S, N+S inner ring, N+S outer ring, N(S), N(S) inner ring and N(S) outer ring. Two methods can be used to determine the resolution of the different detector segments, which are explained in detail in Ref. [18], but will be briefly outlined here. The first method uses the EP angle from two equal multiplicity subevents, (a) and (b), where the resolution of each subevent is

$$\langle \cos[km(\Psi_m^a - \Psi_R)] \rangle = \sqrt{\langle \cos[km(\Psi_m^a - \Psi_m^b)] \rangle} \quad (6)$$

with m denoting the harmonic of the measured EP being used and k is a multiplier such that $n=km$. The resolution of the combined subevents can be determined using

$$\langle \cos[km(\Psi_m - \Psi_R)] \rangle = \frac{\sqrt{\pi}}{2\sqrt{2}} \chi_m \exp(-\chi_m^2/4) \times [I_{(k-1)/2}(\chi_m^2/4) + I_{(k+1)/2}(\chi_m^2/4)] \quad (7)$$

where $\chi_m = v_m \sqrt{2N}$ with v_m being the measured flow signal and $I_{(k-1)}$ and $I_{(k+1)}$ are modified Bessel functions. The second method uses three subevents where the multiplicity of each is not required to be equal. The resolution for this method is calculated by

$$\langle \cos[km(\Psi_m^a - \Psi_R)] \rangle = \sqrt{\frac{\langle \cos[km(\Psi_m^a - \Psi_m^b)] \rangle \langle \cos[km(\Psi_m^a - \Psi_m^c)] \rangle}{\langle \cos[km(\Psi_m^b - \Psi_m^c)] \rangle}} \quad (8)$$

Using the first method with $m=2$, the 2nd and 4th harmonic EP resolutions for the different segments of the RXNP are shown vs. centrality using min-bias events in Fig. 14. In this figure one can see a factor of ~ 2 increase in the 2nd harmonic EP resolution when using the full RXNP detector compared to the BBC, which is what was expected from simulations (see Fig. 2). This factor is even greater ($\sim 4x$) when using the 4th harmonic plane. The 1st harmonic resolution was also examined, but showed inconsistencies, making it unreliable. These inconsistencies included significantly overestimating the EP resolution for central events when using the first method. When using the second method the resolution varied significantly depending upon which of PHENIX's other sub-systems were used in measuring the Ψ_1^b and Ψ_1^c angles. Also, when Ψ_1^b and Ψ_1^c are from each RXNP arm, the resulting resolution of the third detector's EP angle (Ψ_1^a) was significantly underestimated. Possible causes of this behavior include momentum conservation between the two RXNP

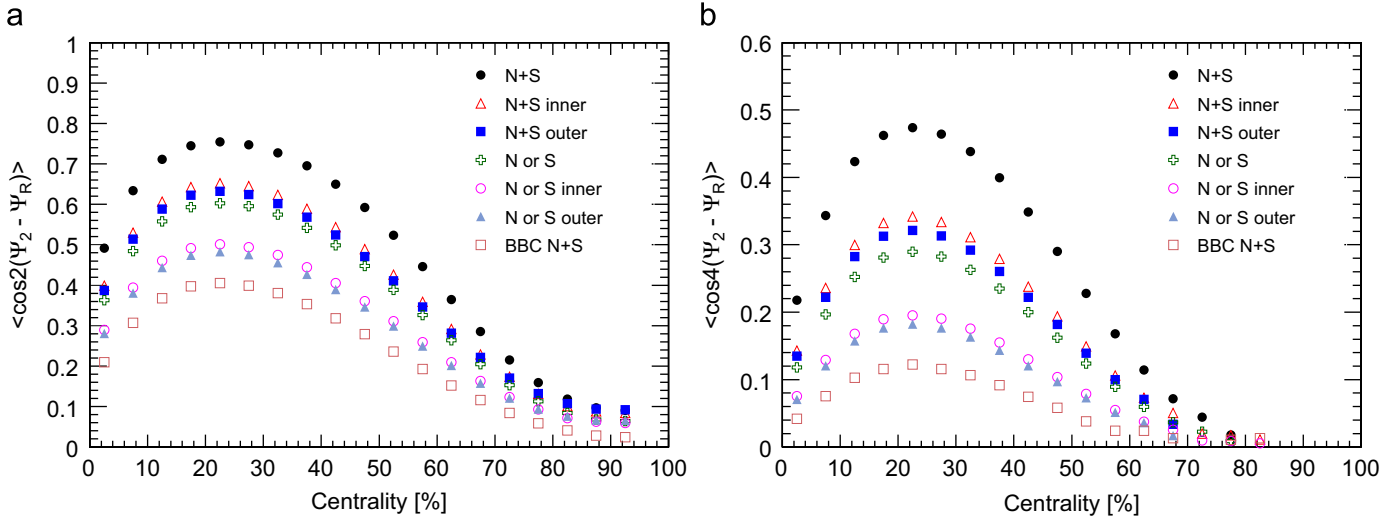


Fig. 14. (a) shows the 2nd harmonic EP resolution for different RXNP detector segments using min-bias events, while (b) is the 4th harmonic. For reference, the corresponding BBC resolution is also shown. Notice (a) and (b) have different size y-axis.

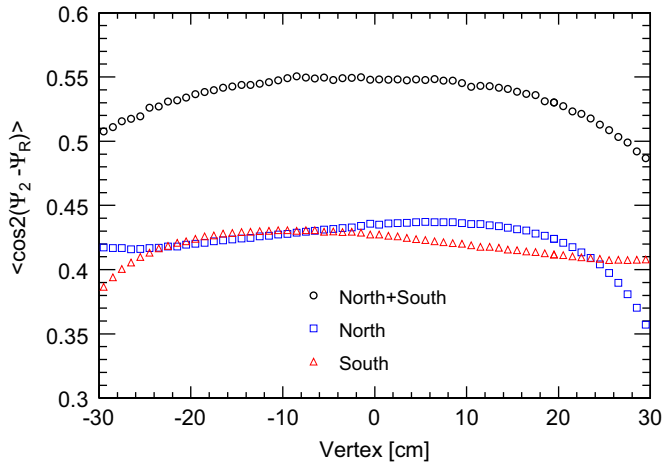


Fig. 15. Second harmonic EP resolution vs. vertex for the south arm (red triangles), north arm (blue squares) and combined arms (black circles) for min-bias events within the PHENIX vertex acceptance of ± 30 cm. The resolution is calculated using the second method (Eq. (8)) where Ψ_2^N and Ψ_2^S are from the BBC north and BBC south when calculating the combined resolution and RXNP opposite arm and BBC N+S when calculating the individual arm resolutions. In all cases $m=2$. (For interpretation of the references to color in this figure legend, the reader is referred to the web version of this article.)

arms and the small 1st harmonic anisotropic flow signal within the RXNP's η coverage [26].

Using the second method (Eq. (8)), where again $m=2$, the RXNP's 2nd harmonic EP resolution is shown vs. vertex in Fig. 15. This figure shows that each detectors' resolution varies by $< 4\%$ within ± 20 cm of the nominal vertex. However, at the edge of PHENIX's vertex acceptance of ± 30 cm the resolution varies by up to 10% for the south arm, 18% for the north and 11% when combined. The effect doubles for the 4th harmonic. For each arm the maximum resolution is achieved at ~ 7 cm closer to the arm than the nominal vertex or ~ 32 cm from each arm.

The decrease in resolution away from this position is the result of a complex interplay between a number of factors. The slow rise in resolution as the vertex approaches a detector arm can largely be explained by the η dependence of v_2 . As shown in Ref. [27], the v_2 , or 2nd harmonic azimuthal particle asymmetry used here to measure the EP, increases as η approaches 0, resulting in a more accurate EP measurement the closer the event vertex is to an arm of the RXNP.

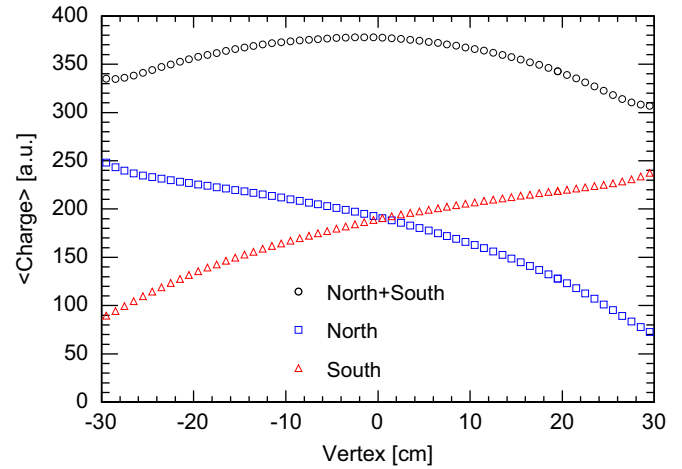


Fig. 16. Mean charge deposited into the RXNP south arm (red triangles), north arm (blue squares) and combined arms (black circles) as a function of collision vertex position for min-bias events. In the case of the individual arms, the charge deposited increases as the event vertex occurs further away. (For interpretation of the references to color in this figure legend, the reader is referred to the web version of this article.)

However, this effect is eventually offset due to the decreasing size of the detector acceptance (smaller η coverage) leading to a smaller multiplicity of particles used in the EP determination, resulting in a less accurate EP and lower resolution.

The change in the observed multiplicity in the RXNP with respect to event vertex is roughly proportional to the change in energy deposition, as seen in Fig. 16. However, it is important to note the closer the event vertex is to an arm, the longer the average path length the particles have passing through the scintillators, which results in more energy being deposited on a per particle basis. This effect acts counter to the loss in energy deposition due to the lower detector multiplicity, making the energy deposition only a guide to how the particle multiplicity changes with event vertex.

6. Conclusion

The PHENIX Collaboration successfully designed, installed and commissioned the RXNP before the 2007 RHIC run to more accurately measure the RP angle of colliding Au nuclei. This detector performed as expected from simulations by increasing PHENIX's

2nd harmonic EP resolution a factor of ~ 2 from the previously used BBC detector. Combined with the recently completed 2010 RHIC run, where almost 2x the number of events were collected than in 2007, this higher resolution detector expands PHENIX's capabilities and allows for analysis of ever rarer particles and more accurate measurements, which has already been demonstrated in several recent articles [22,23,28,29]. The measurements made possible by the improved EP resolution provided by the RXNP further expand the scientific community's understanding of the QGP.

Acknowledgments

We would like to thank the KEK E325 experiment for lending the PMT's used in the RXNP and the PHENIX DAQ team, especially M.L. Purschke and C. Pinkenburg. We also thank A. Franz and J. La Bounty for their help in the magnetic field testing, along with M. Lenz for his many contributions. For the use of Fig. 9 we thank R. Ruggiero and for their contributions we also acknowledge S.P. Stoll, K. Okada and S. Boose.

References

- [1] J.C. Hill, et al., Nucl. Instr. and Meth. A 499 (2003) 469.
- [2] H. Hahn, et al., Nucl. Instr. and Meth. A 499 (2003) 245.
- [3] A. Adare, et al., Phys. Rev. Lett. 98 (2007) 162301.
- [4] B.I. Abelev, et al., Phys. Rev. C 75 (2007) 054906.
- [5] S.S. Adler, et al., Phys. Rev. Lett. 91 (2003) 182301.
- [6] S.S. Adler, et al., Phys. Rev. C 76 (2007) 034904.
- [7] H. Agakishiev, et al., arXiv:1010.0690[nucl-ex].
- [8] K. Adcox, et al., Nucl. Phys. A 757 (2005) 184.
- [9] J. Adams, et al., Nucl. Phys. A 757 (2005) 102.
- [10] B.B. Back, et al., Nucl. Phys. A 757 (2005) 28.
- [11] I. Arsene, et al., Nucl. Phys. A 757 (2005) 1.
- [12] B.I. Abelev, et al., Phys. Rev. Lett. 101 (2008) 252301.
- [13] J. Adams, et al., Phys. Rev. Lett. 92 (2004) 062301.
- [14] B.I. Abelev, et al., Phys. Rev. C 81 (2010) 054908.
- [15] J. Adams, et al., Phys. Rev. Lett. 93 (2004) 012301.
- [16] J. Adams, et al., Phys. Rev. C 71 (2005) 044906.
- [17] S. Afanasiev, et al., Phys. Rev. C 80 (2009) 054907.
- [18] A.M. Poskanzer, S.A. Voloshin, Phys. Rev. C 58 (1998) 1671.
- [19] J.P. Sullivan, et al., Nucl. Instr. and Meth. A 499 (2003) 549.
- [20] C. Woody, et al., in: Proceedings of the Nuclear Science Symposium and Medical Imaging Conference, Orlando, FL, 2009, p. 1002.
- [21] GEANT—Detector Description and Simulation Tool, CERN Program Library Long Write-up W5013, CERN Geneva.
- [22] A. Adare, et al., Phys. Rev. Lett. 105 (2010) 142301.
- [23] A. Adare, et al., Phys. Rev. Lett. 105 (2010) 062301.
- [24] E. Garcia, et al., Nucl. Instr. and Meth. A 474 (2001) 38.
- [25] J. Barrette, et al., Phys. Rev. C 56 (1997) 3254.
- [26] B.B. Back, et al., Phys. Rev. Lett. 97 (2006) 012301.
- [27] B.B. Back, et al., Phys. Rev. C 72 (2005) 051901 (R).
- [28] A. Adare, et al., Phys. Rev. Lett. 104 (2010) 252301.
- [29] A. Adare, et al., arXiv:1010.1521 [nucl-ex].